



# Altered branching patterns of Purkinje cells in mouse model for cortical development disorder

SUBJECT AREAS:

NEUROIMAGING

IMAGING

NEURODEVELOPMENTAL  
DISORDERS

BIOPHYSICS

Jinkyung Kim<sup>1,2</sup>, Namseop Kwon<sup>1,2</sup>, Soeun Chang<sup>1,3</sup>, Kyong-Tai Kim<sup>2,4</sup>, Dongmyeong Lee<sup>5</sup>,  
Seunghwan Kim<sup>5</sup>, So Jeong Yun<sup>2</sup>, Daehee Hwang<sup>2,6</sup>, Jee Woong Kim<sup>7</sup>, Yeukuang Hwu<sup>8</sup>,  
Giorgio Margaritondo<sup>9</sup>, Jung Ho Je<sup>1,2,3</sup> & Im Joo Rhyu<sup>7</sup>

Received  
28 June 2011

Accepted  
3 October 2011

Published  
18 October 2011

<sup>1</sup>X-ray Imaging Center, Pohang University of Science and Technology (POSTECH), Pohang, 790-784, South Korea, <sup>2</sup>School of Interdisciplinary Bioscience and Bioengineering, Pohang University of Science and Technology (POSTECH), Pohang, 790-784, South Korea, <sup>3</sup>Department of Materials Science and Engineering, Pohang University of Science and Technology (POSTECH), Pohang, 790-784, South Korea, <sup>4</sup>Department of Life Science, Division of Molecular and Life Sciences, Pohang University of Science and Technology (POSTECH), Pohang, 790-784, South Korea, <sup>5</sup>APCTP & IES/NCSSL, Department of Physics, Pohang University of Science and Technology (POSTECH), Pohang, 790-784, South Korea, <sup>6</sup>Department of Chemical Engineering, Pohang University of Science and Technology (POSTECH), Pohang, 790-784, South Korea, <sup>7</sup>Department of Anatomy, College of Medicine and Institute of Human Genetics, Korea University, 126-1 Anam-Dong 5-Ga, Sungbuk-Ku, Seoul, 136-705, South Korea, <sup>8</sup>Institute of Physics, Academia Sinica, Nankang, Taipei 11529, Taiwan, <sup>9</sup>Ecole Polytechnique Fédérale de Lausanne (EPFL), CH-1015 Lausanne, Switzerland.

Correspondence and  
requests for materials  
should be addressed to

J.H.J. (jhje@postech.ac.kr) or  
K.T.K. (ktk@postech.ac.kr)

**Disrupted cortical cytoarchitecture in cerebellum is a typical pathology in reeler. Particularly interesting are structural problems at the cellular level: dendritic morphology has important functional implication in signal processing. Here we describe a combinatorial imaging method of synchrotron X-ray microtomography with Golgi staining, which can deliver 3-dimensional (3-D) micro-architectures of Purkinje cell (PC) dendrites, and give access to quantitative information in 3-D geometry. In reeler, we visualized in 3-D geometry the shape alterations of planar PC dendrites (i.e., abnormal 3-D arborization). Despite these alterations, the 3-D quantitative analysis of the branching patterns showed no significant changes of the  $77 \pm 8^\circ$  branch angle, whereas the branch segment length strongly increased with large fluctuations, comparing to control. The 3-D fractal dimension of the PCs decreased from 1.723 to 1.254, indicating a significant reduction of dendritic complexity. This study provides insights into etiologies and further potential treatment options for lissencephaly and various neurodevelopmental disorders.**

The formation of cellular layers and dendritic architectures is essential in the development of cortical structures in the mammalian brain<sup>1</sup>. Alterations in cortical structures are related to epilepsy, mental retardation, deficits in learning and memory, autism, and schizophrenia<sup>2-4</sup>. The alteration patterns of cortical structures are often studied using neurological mutation reeler<sup>5</sup>, which is characterized by ataxia, tremors, imbalance, and a reeling gait<sup>6-9</sup>. In the reeler cerebellum, the cytoarchitecture of neural networks and neurons becomes gradually defective during the developmental process<sup>10,11</sup>. The Purkinje cells (PCs) are not arranged in a regular plane but clustered in subcortical areas at early stages of corticogenesis. As a consequence of the ectopic location of such cells, an aberrant laminar organization occurs<sup>12,13</sup>.

Previous investigations of the alteration patterns of cortical structures were based on imaging methods including light microscopy (LM), electron microscopy (EM), X-ray computer-assisted tomography (CT) and magnetic resonance imaging (MRI). For example, LM histological investigations of the reeler brain revealed abnormal cytoarchitecture in cerebral and cerebellar cortices and in the hippocampus<sup>11,14-17</sup>. MRI analyzed the neuromorphology such as the quantification of the general sizes of brain and cerebellum<sup>18</sup>. However, the subcellular-level alteration patterns including dendritic abnormalities are still largely unexplored.

Here we present an alternate strategy that can deliver not only the 3-dimensional (3-D) micro-architecture of cerebellar tissue but also that of single neurons, and give access to quantitative information in 3-D geometry. This approach combines synchrotron X-ray microscopy (Fig. 1) with Golgi staining<sup>19,20</sup>. Microscopy based on phase contrast and strongly collimated synchrotron hard X-rays<sup>21-23</sup> produces images of very high quality with limited doses. Furthermore, hard X-rays are highly penetrating and can examine thick specimens with high resolution as

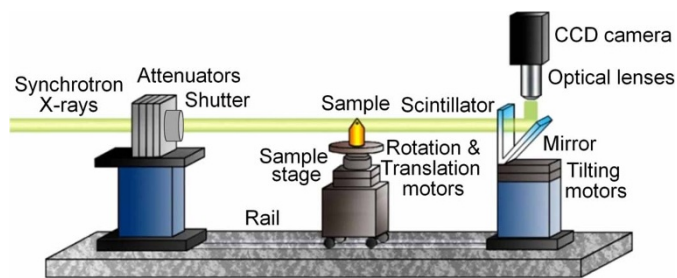


**Figure 1** | Scheme of the synchrotron X-ray microscopy apparatus.

required here<sup>24</sup>. To increase the contrasts and analyze minute details, we used Golgi staining by impregnating fixed tissues with potassium dichromate and silver nitrate. The heavy metals of the Golgi staining enhance the X-ray absorption contrast. This approach can explore microscopic details in very thick (up to 5 mm or more) specimens and reveal subcellular-level alteration patterns<sup>24,25</sup>.

## Results

**3-D Neuronal Micro-Architecture of Whole Cerebellum.** We first acquired radiographs over a large field of view, then progressively zoomed into more detailed pictures. Figure 2 shows typical results in a normal mouse, starting from the entire cerebellum and then focusing down to local dendrites. The progressive zoom (box in Fig. 2A) clearly reveals the 4-layer arrangement (Fig. 2B) and the network of different types of neurons and glia (Fig. 2C), as well as finely detailed PC dendrites (Fig. 2D).

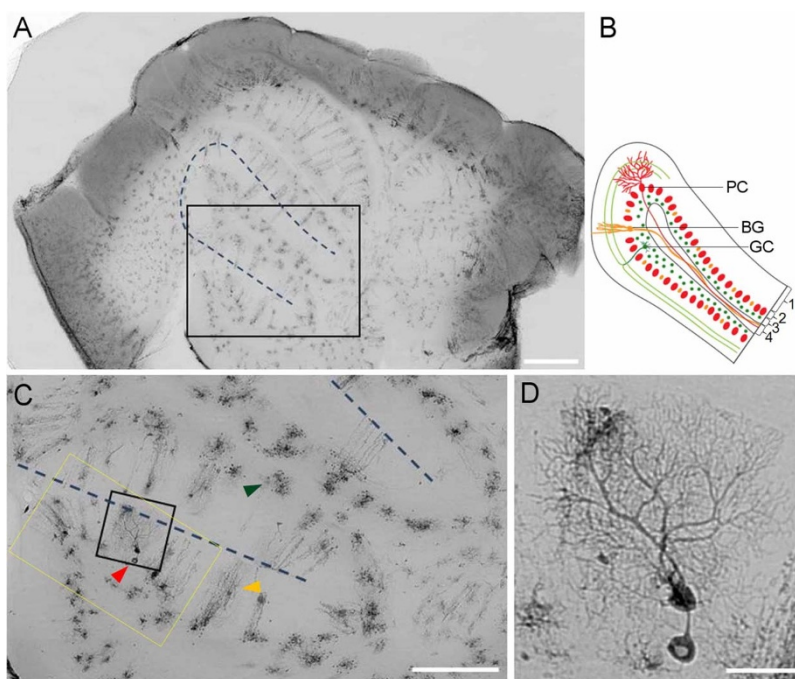
In addition to the projection images, we performed microtomography of the cerebellar tissue (the yellow box in the Fig. 2C) and could observe in 3-D the realistic neuronal network (Fig. 3A; supplemental video 1). Well-aligned PCs tend to be oriented towards the external cerebellum surface (arrow heads in Fig. 3A). Different types of neurons and glia establish the correct neural circuit. On the contrary, in the reeler cerebellum the PCs do not form a well-defined layer and are not aligned in the same direction: this can be seen in the

reconstructed tomographic image of Figure 3B (supplemental video 2). The PCs tend to have a random orientation (arrow heads in Fig. 3B).

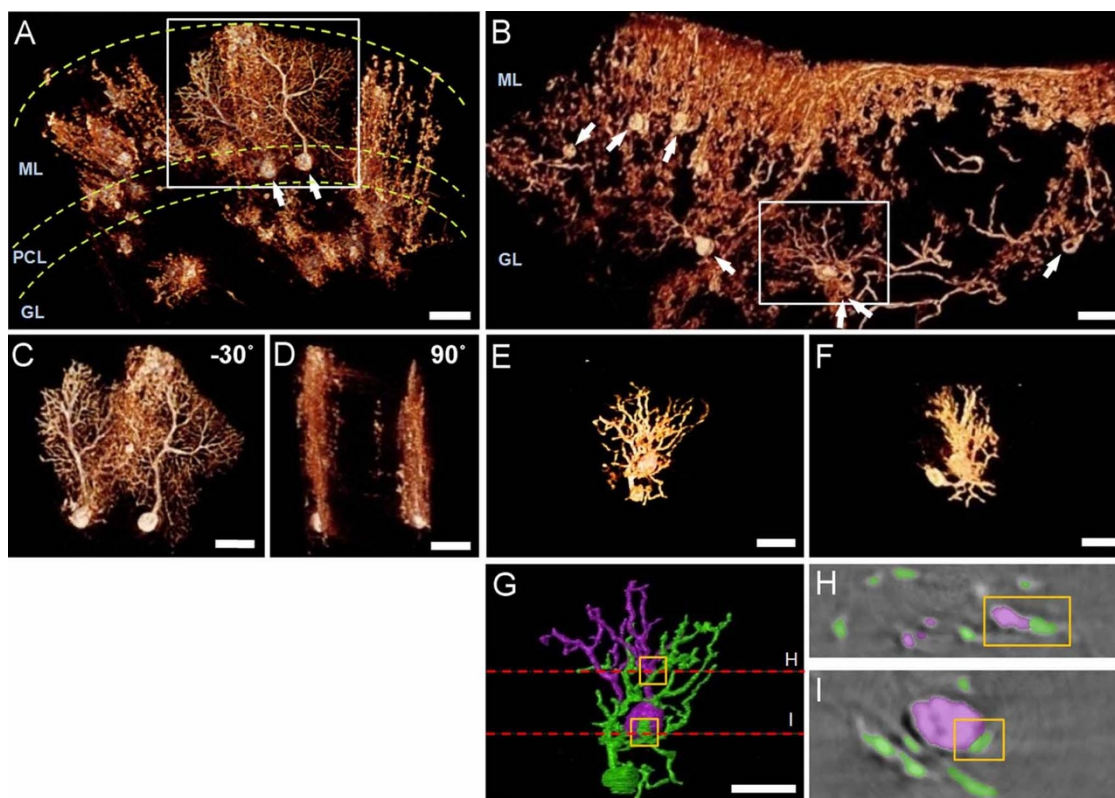
**Microtomographic Images Showing Altered Arborizations of Reeler PCs.** 3-D volume rendered images of normal PCs are shown in Figure 3C and D whereas Figure 3E and F picture reeler cells (corresponding to the boxes of Fig. 3A and B). Highly branched cells with a flat system of dendritic arbors are clearly seen (Fig. 3C and D). Figure 3D also shows that the PCs are oriented parallel to the coronal plane (supplemental video 3).

In sharp contrast, Figure 3E and F show that the reeler PC arborization is not flat and not oriented but developed in 3-D (supplemental video 4). Furthermore, the overall length of each cell is significantly small in reeler mice, indicating a reduction of the dendritic development. Interestingly, the two cells of Figure 3E and F are abnormally neighbored to each other. As demonstrated in the segmented image of Figure 3G (supplemental video 5), the two slice images (Fig. 3H and I) at the dotted lines of Figure 3G show that the dendrites of one cell (green) look connected not only to the dendrites of the other (violet) (box in Fig. 3H) but also to its soma (box in Fig. 3I).

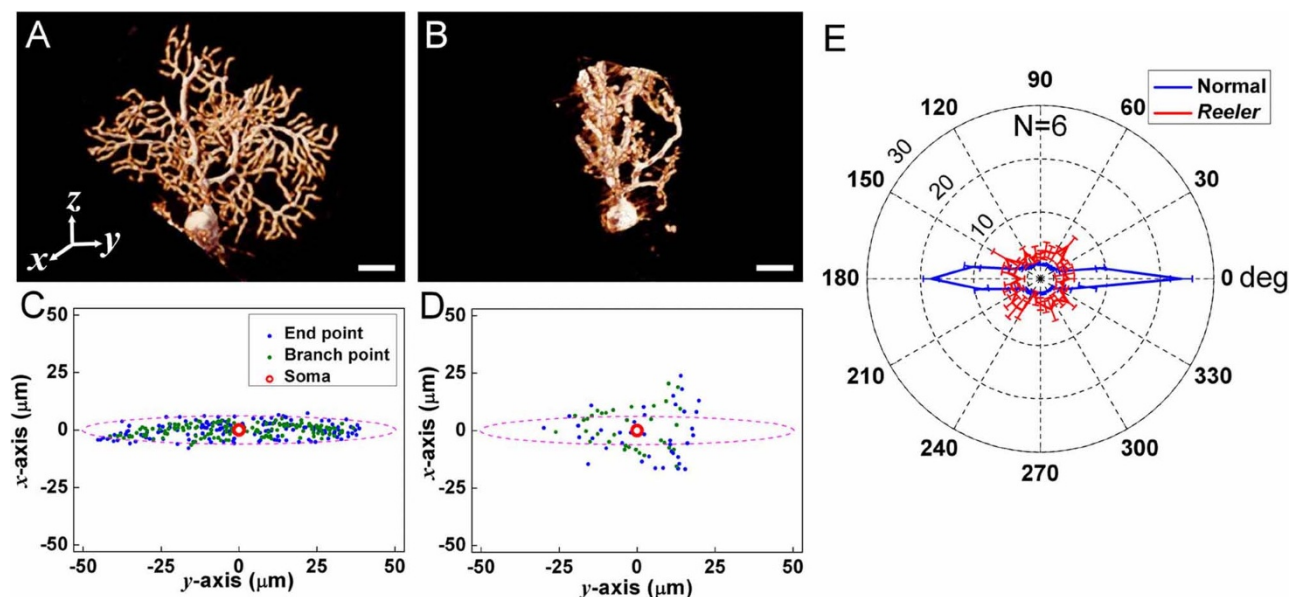
**Quantitative Analysis of the Shape Alterations.** Analysis of the branching patterns of neurons is important for understanding their functions<sup>26,27</sup>. From the 3-D volume-rendered images of a normal (Fig. 4A; supplemental video 6) and a reeler (Fig. 4B; supplemental video 7) PCs, we measured the distribution of the projections of end points (blue dots) and branch points (green dots) into the  $x$ - $y$  transverse plane, as shown in Figure 4C and D, respectively. For the normal cell, the projections are close to the  $y$ -axis, so the dendrite system is flat and close to the sagittal plane. For the reeler cell, this flat character is not remarked. Statistically the arbor span, the width, and the height of PCs are  $82.9 \pm 2.5 \mu\text{m}$ ,  $13.9 \pm 1.5 \mu\text{m}$ , and  $79.9 \pm 5.4 \mu\text{m}$  (mean  $\pm$  SEM), respectively, as directly measured for six normal mice in 3-D geometry (Table 1). The arbor span (the



**Figure 2** | Microradiograph of a normal mouse cerebellum. (A) Patched image of the entire cerebellum (300  $\mu\text{m}$ ). The dashed line marks one lobule, consistent with the scheme in (B). (B) Lobule scheme. PC, Purkinje cell; BG, Bergmann glial cell; GC, granule cell; note the 4 layers: 1, molecular layer; 2, PC layer; 3, granular layer; 4, white matter. (C) Magnified image of the box region in (A) (red, orange, and green arrowheads: Purkinje, Bergmann glia, and granule cells). (D) Magnified image of the black box region in (C). (Scale bars: A, 600  $\mu\text{m}$ ; C, 300  $\mu\text{m}$ ; D, 50  $\mu\text{m}$ .)



**Figure 3** | 3-D tomographic volume-rendered images of cerebellar tissues. (A) 3-D network of cerebellar neurons (the yellow box in the Fig. 2C). The bodies of two PCs are marked by white arrow heads. ML, molecular layer; PCL, PC layer; GL, granular layer (supplemental video 1). (B) Disrupted neural circuit in a reeler cerebellum (300  $\mu$ m). PCs are randomly oriented (supplemental video 2). (C) Alignment of two PCs in a normal cerebellum (white box in (A)) (point of view:  $-30^\circ$  from the direction perpendicular to the sagittal plane). The highly branched cells with planar dendritic arborizations are aligned to each other. A detailed analysis reveals that a Bergmann glial cell coexists with the PC on the right (supplemental video 3). (D) The same cells as in (C), from a point of view in the sagittal plane: they are markedly parallel each other. Their common orientation is parallel to the coronal plane. (E and F) Disrupted alignment of two PCs in a reeler cerebellum (white box in (B)), from two different points of view (supplemental video 4). (G) Structures of (E) obtained by segmentation. (H and I) Slice images at the red dotted lines in (G). The yellow boxes represent slice images of the corresponding boxed areas in (G). The dendrites of one cell (green) are connected not only to the dendrites of the other (violet) (yellow box in (H)) but also to its soma (yellow box in (I)). (supplemental video 5). (Scale bars: 50  $\mu$ m).



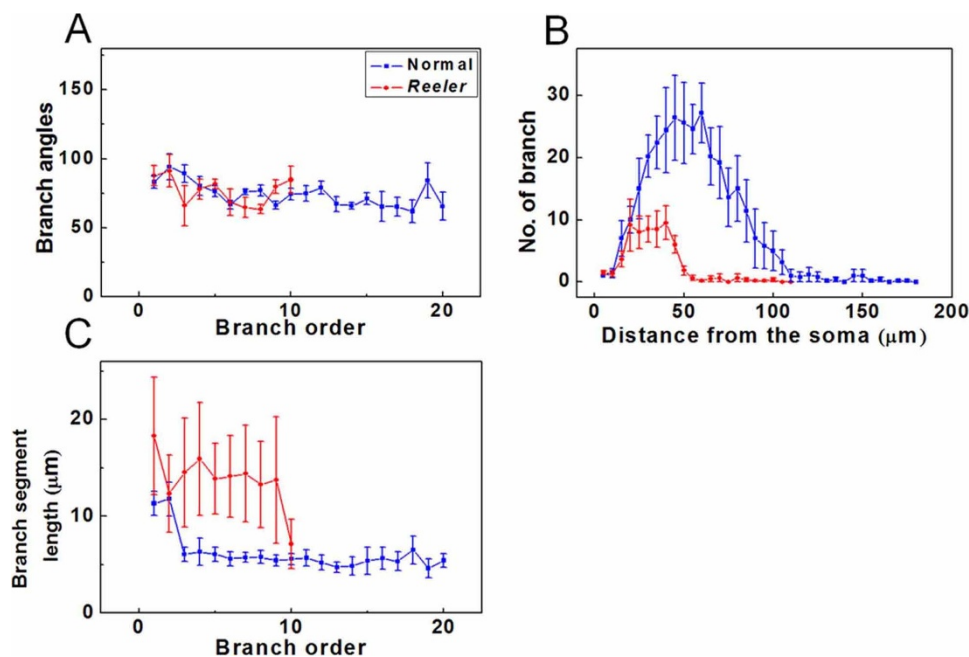
**Figure 4** | Quantitative characterization of shape alterations in reeler PCs. (A) 3-D tomographic volume-rendered image of a normal (flat) PC (supplemental video 6). Here,  $y$ - $z$  defines the sagittal plane,  $x$ - $z$  the coronal plane and  $x$ - $y$  the transverse plane. (B) volume-rendered image of a reeler cell, showing the shape alterations with respect to the normal case (supplemental video 7). (C) Projections on the  $x$ - $y$  plane of dendrite end points (blue dots) and branch points (green dots). The soma is marked by a red circle at the origin. (D) Similar projections for the altered reeler dendritic structure. (E) Angular distribution in the  $x$ - $y$  plane of dendrite end points and branch points together, for six normal (blue) and six reeler (red) mice. The plot shows the percentage of points found in each 10-degree angular interval (the errors correspond to the s.e.m.). Scale bars: A and B, 20  $\mu$ m.



Table 1 | Sizes of PCs, measured for six normal and six reeler mice in 3-D geometry.

	Soma size ( $\mu\text{m}$ )	Arbor span ( $\mu\text{m}$ )	Width ( $\mu\text{m}$ )	Height ( $\mu\text{m}$ )	N
<b>Normal Purkinje cell</b>	$21.2 \pm 1.1$	$82.9 \pm 2.5$	$13.9 \pm 1.5$	$79.9 \pm 5.4$	6
<b>Reeler Purkinje cell</b>	$22.3 \pm 1.5$	$40.0 \pm 4.6$	$28.7 \pm 4.8$	$43.5 \pm 3.3$	6

Values are the mean  $\pm$  SEM for six cells.



**Figure 5** | 3-D quantitative analysis of branching patterns of normal and reeler PCs. (A) Branch angles ( $P = 0.675$ ). (B) 3-D Sholl analysis of the distance of the terminal tip from the soma ( $P = 0.116 \times 10^{-3}$ ). (C) Branch segment length ( $P = 0.17 \times 10^{-3}$ ). The errors correspond to the s.e.m. (number of tested mice  $n = 6$  for each case).

height) reduces to  $40.0 \pm 4.6 \mu\text{m}$  ( $43.5 \pm 3.3 \mu\text{m}$ ) while the width increases to  $28.7 \pm 4.8 \mu\text{m}$  for six reeler cells (Table 1). To compare these two cases quantitatively, we computed the 99% confidence volume for six normal mice using Hotelling's  $T^2$  statistic<sup>28</sup>; the result is shown by the magenta dotted line in Figure 4C. In contrast, the distribution for the reeler cell of Figure 4D has a statistically significant portion of points ( $51 \pm 3\%$ ) (mean  $\pm$  SEM) well outside this confidence volume.

In essence, both the visual inspection and the statistical analysis<sup>29</sup> reveal that reeler PCs exhibit abnormally large arborizations perpendicular to the sagittal plane and reduced arborizations in the same plane. These conclusions are confirmed by the angular distribution of the branch and end points (Fig. 4E); note that the angular distribution for reeler mice is essentially random. Interestingly, the soma size is not altered as  $22.3 \pm 1.5 \mu\text{m}$  (Table 1), suggesting that reelin is not related to soma morphogenesis during the cell development.

#### Branching Rules of PCs Revealed by 3-D Quantitative Analysis.

This analysis detected further interesting differences between normal and reeler cells, not immediately evident from the raw images. We found that the branch angles for normal PCs are almost the same and equal to  $74 \pm 6^\circ$  (mean  $\pm$  SEM) for all the branch points from the soma to the end of the dendritic system (Fig. 5A) and for all six tested normal mice. The same conclusion applies to six reeler cells with the branch angles of  $77 \pm 8^\circ$ , which is not statistically different from that of normal mice. Thus, the abnormal arborization in reeler mice does not appear to influence the branch angles.

In contrast, the Sholl analysis<sup>30</sup> in 3-D (Fig. 5B) shows that the branch number is significantly reduced in reeler cells. This indicates a

reduced arbor density. Figure 5B reveals another interesting feature by showing the total number of branch points of each cell. This number is much smaller for reeler than for normal cells. The same figure shows that the distance between the soma and the end of the dendritic system is shorter.

Furthermore, Figure 5C shows that the branch segment length – the distance from one branch point to the next – is much larger for reeler cells than for normal cells. In the latter case, the branch segment length is above  $10 \mu\text{m}$  for the 1<sup>st</sup> and 2<sup>nd</sup> branch points from the soma; for the subsequent branching, it becomes constant for all branches and all normal mice, with a value of  $5.6 \pm 0.9 \mu\text{m}$ . For the reeler mice, after the first branch point the length is significantly larger,  $13.4 \pm 4.7 \mu\text{m}$  and with large fluctuations.

**3-D Fractal Dimension.** This parameter reflects the degree of geometric complexity<sup>31</sup> of the PC branching systems. Previous estimates from 2-D data varied among different authors<sup>31–34</sup>. We extracted our values using instead 3-D data with the box counting method. The results for normal and reeler PCs were  $1.71 \pm 0.03$  and  $1.25 \pm 0.02$  (Table 2). Our fractal dimension for normal cells is consistent

Table 2 | The fractal dimension of PCs in three dimension.

	D	SD	N
<b>Normal Purkinje cell</b>	1.71	0.03	6
<b>Reeler Purkinje cell</b>	1.25	0.02	6

The box-counting method is used to estimate the Fractal dimension  $D$  with a standard deviation  $SD$  for six cells.



with previous results<sup>31,32,34</sup>, whereas for reeler cells it is significantly smaller, indicating a reduced geometric complexity. The lower geometric complexity is also consistent with the data of Figure 5 and could reflect reduced synaptic connections with other neurons.

## Discussion

This study provides accurate, 3-D quantitative descriptions of branching patterns of Purkinje cells in reeler and normal mice based on a new combinatorial imaging method of synchrotron X-ray microtomography with Golgi staining.

Our work has two different kinds of important implications: first, the demonstration of the experimental technique and the possibility to extend it to other cases, which requires a realistic analysis of the limitations. Second, the specific results and their significance in the general context of the assessment of the reeler model.

As far as the technique is concerned, we basically demonstrated that the combination of synchrotron X-ray microimaging and Golgi staining can reveal the 3-D micro-architecture of cerebellar tissues at the cellular and subcellular levels with high absolute accuracy compared to alternate techniques<sup>35,36</sup>. Furthermore, it can analyze thick specimens, up to several mm, thanks to high penetration capability of hard X-rays<sup>24,25</sup>. The results presented here provide ample evidence of the feasibility of this strategy. To what other domains can this approach be applied? In principle, any cellular system with complex microscopic geometry could profit from its performances. This specifically applies to neuron systems such as the hippocampus or the cerebral cortex. Preliminary results in these directions are quite promising and confirm the indications of the present tests.

The basis for radiation damage to mammalian cells has been extensively studied; however a clear understanding of how much radiation doses kill and mutate cells has yet to emerge. In our research, the high contrast made possible by the superior characteristics of the synchrotron source and by Golgi staining keeps the X-ray doses to a low level. We also certificated that radiation doses for tomography (actual dose; 100sec/ tomography) did not produce any detectable damage. The tests with increasing total dose to the point of detecting damage effects specifically enabled us to verify that the results used in this article are not affected by damage problems.

Another key issue in our technique is reaching a good compromise between phase contrast and staining-enhanced absorption contrast. The two contrast mechanisms are related to each other, in particular when staining is used. Specifically, staining to reach high absorption could suppress the phase contrast that requires sufficient transmission through the sample. There is no general rule to find a compromise and the corresponding optimum level of staining, since the two contrast mechanisms work in different ways for different specimens and for different parts of the same specimens. The only solution is to use empirical preliminary tests of Golgi staining to find the optimal conditions.

At present, clinical application of synchrotron radiation CT examination might be more difficult than that of dynamic contrast-enhanced CT<sup>37–39</sup> on account to both the limited availability of synchrotron X-ray (large, expensive facilities) and the compromise between multi-section imaging and a fast data acquisition time. Nevertheless, the medical applications of synchrotron sources<sup>40–44</sup> have showed the possibility of improving in diagnostic accuracy with reduced radiation dose to the patients<sup>45</sup>. It is likely that over the next few years, compact and intense X-rays that operate in the hard x-ray regime (15–150 keV) will enable access to practical diagnostic imaging devices<sup>46</sup>.

We can now move to the discussion of our specific results. Accurate analysis of neuronal branching patterns is important because of their association with synaptic connections to other neurons<sup>47,48</sup>. The structural information on reeler has been limited in 2-D geometry so far. By our accurate, 3-D quantitative analysis, we show substantial geometric differences in reeler cells, demonstrated by

branching rules, fractal dimension and quantitative analysis of 3-D arborization, comparing to flat dendritic system in normal cell.

More specifically, the abnormal arborization perpendicular to the sagittal plane and the reduced arborization on the same plane are likely to make it more difficult to form synapses between PCs and the other cerebellar neurons – known to have a potent excitatory or inhibitory effect on postsynaptic spiking of a cerebellar folium<sup>49</sup>. In addition, the anomalous connections between reeler PCs could conceivably affect the functionality of the reeler cerebellum. Moreover, the reduced geometrical complexity of the reeler dendritic structures, revealed by the fractal dimension, is also likely to decrease the probability of synaptic connections with other neurons, enhancing the above effects. Such differences stress the difficulty of reeler cells to establish appropriate neural networks, resulting in their malfunction, so could be a significant factor in understanding the disease model.

Lissencephaly (a severe developmental disorder in which neuronal migration is impaired), for instance, is associated with human reelin mutation<sup>50</sup>. Structural aberrations of patients with lissencephaly is correspondent to those of reeler because of their highly conserved functions<sup>50–53</sup>. Our accurate quantitative results of dendritic altered features of reeler in 3-D provide insights into etiologies and further potential treatment options for lissencephaly as well as for various neurodevelopmental disorders including the Alzheimer disease, schizophrenia, autism and epilepsy<sup>6,7,9</sup>.

## Methods

**Animals.** Mice with the control genotype, B6C3Fe-*a/a*<sup>+/+</sup>, or mutant genotypes, B6C3Fe-*a/a-Reln*<sup>fl/Reln</sup> (reeler) were housed at POSTECH in a constant-temperature room with a 12-h light/dark cycle. All mouse lines were maintained in specific pathogen-free conditions at the POSTECH animal facility under institutional guidelines.

**Tissue preparation.** The mice (age 150–180 days) were anesthetized with ketamine/rompun before perfusion with PBS and 4% PFA. After perfusion, the cerebella were placed into freshly made 2.5% potassium dichromate (4-days) and 0.75% silver nitrate (3-days) solutions at room temperature in the dark (Golgi staining procedure). After dehydrated and embedded in resin (epon 812 kit; EMS, Hatfield, PA, USA), each cerebellum was sliced using a sliding microtome (SM2000R; Leica, Nussloch, Germany) from 0.1 to 5.0 mm thicknesses.

**Synchrotron X-ray imaging.** Experiments were performed on the ICPCIR (International Consortium of Phase Contrast Imaging and Radiology) at 7B2 synchrotron X-ray microscopy high flux beamline (10–60 keV energy range) of the PLS (Pohang Light Source: 2.5 GeV) and at BL01A X-ray microscopy beam line (5–35 keV energy range) of NSRRRC (National Synchrotron Radiation Research Center: 1.5 GeV). Figure 1 shows the experimental setup of the X-ray imaging system. In order to control and block the intensity of the X-ray beam, attenuators and a mechanical shutter with a Pt-Ir blade were used. Sample was mounted on a high precision motor-controlled stage with rotational, tilting, and translational resolutions of 0.002°, 0.0009°, and 250 nm, respectively. A single image was recorded in 100ms. After passing through the sample, the transmitted X-ray beam was converted by a scintillator (CdWO<sub>4</sub>; Nihon Kessho Koogaku Co. Ltd., Hinata Tatebayashi-City Gunma, Japan) to visible light that was then reflected by a mirror and magnified by an optical lens. After magnification, the image was captured by a CCD camera.

**3-D images acquisition and reconstruction.** Several images were averaged into one comprehensive picture at every 0.18° rotation step, calibrated with background images. This process was repeated 1000 times. The projected image set was reconstructed by four parallel computers equipped with the standard filter-back projection reconstruction algorithm. Reconstructed slices consist of 1600 × 1600 pixels in the horizontal and vertical directions. Vertically stacked 2D slices were reconstructed as volume-rendered 3D images using the *Amira*5.2 software (Visage Imaging, San Diego, CA, USA).

**Quantitative analysis.** The main criterion to identify PC among various cell types is the typical soma size (about 20 μm; see Table 1) in normal and reeler cerebella: the soma sizes of the other cell types in the cerebella are generally much smaller than 10 μm. In order to obtain the 3-D coordinates, reconstructed image stacks of PCs were manually segmented and skeletonized using the *Amira*5.2 software. The 3-D coordinates of PCs were automatically analyzed with a *Matlab* software (Mathworks, Natick, MA, USA). For 3-D Sholl analysis (Fig. 5B), a series of concentric spheres of 5 μm increments was drawn around the cell body, and the numbers of branch points between spheres were counted.

**Statistical analysis.** To quantitatively compare dendritic branching patterns from normal and reeler cells, we computed the statistical boundary within which both end



and branch points of cells from all normal tested mice ( $n = 6$ ) reside, and then analyzed the question of whether the end and branch points from the reeler mouse cells are similarly distributed using the following statistical approach:

- (i) To remove experimental and technical variability in each sample, we first normalized so that the data from each normal specimen  $i$  have the mean of end and branch points ( $\text{mean}[x,y]$  where  $(x,y)$  is the coordinate of end and branch points in each sample) at the origin in each sample on the transverse  $x-y$  plane; ii) the same condition applies to the median absolute deviation ( $\text{MAD} = \text{median}[(x,y) - \text{median}[x,y]]$ ), and iii) the soma is located in the origin.
- (ii) After superimposing the normalized distributions of end and branch points from normal cells, we computed the 99% confidence volume of the distributions using Hotelling's  $T^2$  statistic, based on the assumption that the end and branch points are normally distributed around the soma. From this confidence volume, we estimated the sagittal to coronal aspect ratio of the distribution to be 8.2; this parameter is defined as the length ratio of the long and short axes (i.e. square-rooted eigenvalues of the covariance matrix in Hotelling's  $T^2$  statistic) of the ellipsoidal confidence volume.
- (iii) Finally, we compared the distributions of the end and branch points from reeler and normal cells by superimposing the reeler distribution over the control volume obtained for normal cells, after normalizing it so as to have the soma at the origin. By counting the percentage of end and branch points located outside the confidence volume, we quantitatively evaluated the difference between the normal and reeler dendritic branching patterns.

For statistical comparison of three different measures – branch angles, the number of branches, and branch segment lengths – from normal and reeler cells, we tested the null hypothesis that each measure follows the same distribution using the two-sample Kolmogorov-Smirnov (KS) test. For this, we only used data points available for both normal and reeler cells.

**Fractal dimension.** To estimate the fractal dimension of the PCs, we used the box-counting method. First, we embedded the data points of the PCs in the 3-D space. This space was divided in a grid of boxes with size  $r$  and we counted the number of boxes  $N(r)$  that contain at least one data point. A log-log plot of  $r$  versus  $N(r)$  could be fitted by a straight line with slope  $-D$ , where  $D$  is the fractal dimension (supplemental Fig. 1). A linear least square regression was performed to accurately evaluate this slope. To determine the scaling region and the slope, two end-points of the size giving the best linear fits were selected.

1. Whitford, K. L., Dijkhuizen, P., Polleux, F. & Ghosh, A. Molecular control of cortical dendrite development. *Annu Rev Neurosci* **25**, 127–149 (2002).
2. Beckmann, H. Developmental malformations in cerebral structures of schizophrenic patients. *Eur Arch Psychiatry Clin Neurosci* **249 Suppl 4**, 44–47 (1999).
3. Levitt, P. Developmental neurobiology and clinical disorders: lost in translation? *Neuron* **46**, 407–412 (2005).
4. McManus, M. F. & Golden, J. A. Neuronal migration in developmental disorders. *J Child Neurol* **20**, 280–286 (2005).
5. D'Arcangelo, G. *et al.* A protein related to extracellular matrix proteins deleted in the mouse mutant reeler. *Nature* **374**, 719–723 (1995).
6. D'Arcangelo, G. Reelin mouse mutants as models of cortical development disorders. *Epilepsy Behav* **8**, 81–90 (2006).
7. Herz, J. & Chen, Y. Reelin, lipoprotein receptors and synaptic plasticity. *Nat Rev Neurosci* **7**, 850–859 (2006).
8. Lambert de Rouvroit, C. & Goffinet, A. *The reeler mouse as a model of brain development*. (Springer, Berlin, ; New York; 1998).
9. Curran, T. & D'Arcangelo, G. Role of reelin in the control of brain development. *Brain Res Brain Res Rev* **26**, 285–294 (1998).
10. D'Arcangelo, G. & Curran, T. Reeler: new tales on an old mutant mouse. *Bioessays* **20**, 235–244 (1998).
11. Katsuyama, Y. & Terashima, T. Developmental anatomy of reeler mutant mouse. *Dev Growth Differ* **51**, 271–286 (2009).
12. Caviness, V. S., Jr. & Rakic, P. Mechanisms of cortical development: a view from mutations in mice. *Annu Rev Neurosci* **1**, 297–326 (1978).
13. Goffinet, A. M., So, K. F., Yamamoto, M., Edwards, M. & Caviness, V. S., Jr. Architectonic and hodological organization of the cerebellum in reeler mutant mice. *Brain Res* **318**, 263–276 (1984).
14. Caviness, V. S., Jr. Patterns of cell and fiber distribution in the neocortex of the reeler mutant mouse. *J Comp Neurol* **170**, 435–447 (1976).
15. Mikoshiba, K. *et al.* Developmental studies on the cerebellum from reeler mutant mouse in vivo and in vitro. *Dev Biol* **79**, 64–80 (1980).
16. Mariani, J., Crepel, F., Mikoshiba, K., Changeux, J. P. & Sotelo, C. Anatomical, physiological and biochemical studies of the cerebellum from Reeler mutant mouse. *Philos Trans R Soc Lond B Biol Sci* **281**, 1–28 (1977).
17. Heckroth, J. A., Goldowitz, D. & Eisenman, L. M. Purkinje cell reduction in the reeler mutant mouse: a quantitative immunohistochemical study. *J Comp Neurol* **279**, 546–555 (1989).
18. Badaea, A., Nicholls, P. J., Johnson, G. A. & Wetzel, W. C. Neuroanatomical phenotypes in the reeler mouse. *Neuroimage* **34**, 1363–1374 (2007).

19. Friedland, D. R., Los, J. G. & Ryugo, D. K. A modified Golgi staining protocol for use in the human brain stem and cerebellum. *J Neurosci Meth* **150**, 90–95 (2006).
20. Golgi, C. *Sulla fina anatomia degli organi centrali del sistema nervoso*. (Giunti, Firenze; 1995).
21. Hwu, Y. *et al.* Synchrotron microangiography with no contrast agent. *Physics in Medicine and Biology* **49**, 501–508 (2004).
22. Hwu, Y. *et al.* Imaging cells and tissues with refractive index radiology. *Biophysical Journal* **87**, 4180–4187 (2004).
23. Hwu, Y., Tsai, W. L., Grosio, A., Margaritondo, G. & Je, J. H. Coherence-enhanced synchrotron radiology: simple theory and practical applications. *J Phys D Appl Phys* **35**, R105–R120 (2002).
24. Margaritondo, G., Hwu, Y. & Je, J. H. Synchrotron light in medical and materials science radiology. *Riv Nuovo Cimento* **27**, 1–40 (2004).
25. Je, J. H., Weon, B. M., Hwu, Y. & Margaritondo, G. Phase contrast X-ray imaging. *Int J Nanotechnol* **3**, 280–297 (2006).
26. Miller, J. P. & Jacobs, G. A. Relationships between neuronal structure and function. *J Exp Biol* **112**, 129–145 (1984).
27. Spruston, N. Pyramidal neurons: dendritic structure and synaptic integration. *Nat Rev Neurosci* **9**, 206–221 (2008).
28. Richard, A. Johnson, D. W. W. *Applied Multivariate Statistical Analysis*. (Prentice Hall, USA; 2001).
29. Massey, F. J. The Kolmogorov-Smirnov Test for Goodness of Fit. *Journal of the American Statistical Association* **46**, 68–78 (1951).
30. Sholl, D. A. Dendritic organization in the neurons of the visual and motor cortices of the cat. *J Anat* **87**, 387–406 (1953).
31. Smith, T. G., Jr., Lange, G. D. & Marks, W. B. Fractal methods and results in cellular morphology—dimensions, lacunarity and multifractals. *J Neurosci Methods* **69**, 123–136 (1996).
32. Krauss, B. R., Krauss, B. R., S. B. J., Krauss, B. R., S. B. J., Chialvo, D. R., Krauss, B. R., S. B. J., Chialvo, D. R., Apkarain, A. V. Dendritic complexity and the evolution of cerebellar Purkinje cells. *Fractals* **2**, 95–102 (1994).
33. Smith, T. G., Jr., Brauer, K. & Reichenbach, A. Quantitative phylogenetic constancy of cerebellar Purkinje cell morphological complexity. *J Comp Neurol* **331**, 402–406 (1993).
34. Takeda, T., Ishikawa, A., Ohtomo, K., Kobayashi, Y. & Matsuoka, T. Fractal dimension of dendritic tree of cerebellar Purkinje cell during onto- and phylogenetic development. *Neurosci Res* **13**, 19–31 (1992).
35. Kalender, W. A. CT: the unexpected evolution of an imaging modality. *Eur Radiol* **15 Suppl 4**, D21–24 (2005).
36. Tyszka, J. M., Fraser, S. E. & Jacobs, R. E. Magnetic resonance microscopy: recent advances and applications. *Curr Opin Biotechnol* **16**, 93–99 (2005).
37. Johnson, T. R. *et al.* Dual-source CT for chest pain assessment. *Eur Radiol* **18**, 773–780 (2008).
38. Kinahan, P. E., Alessio, A. M. & Fessler, J. A. Dual energy CT attenuation correction methods for quantitative assessment of response to cancer therapy with PET/CT imaging. *Technol Cancer Res Treat* **5**, 319–327 (2006).
39. Ruzsics, B. *et al.* Images in cardiovascular medicine. Myocardial ischemia diagnosed by dual-energy computed tomography: correlation with single-photon emission computed tomography. *Circulation* **117**, 1244–1245 (2008).
40. Burattini, E., Gambaccini, M., Indovina, P. L., Pocek, M. & Simonetti, G. [Synchrotron radiation: a new source in x-ray mammography]. *Radiol Med* **84**, 181–188 (1992).
41. Lewis, R. Medical applications of synchrotron radiation x-rays. *Phys Med Biol* **42**, 1213–1243 (1997).
42. Nachaleil, E. D. F., Garrett RF Monochromatic computed tomography of the human brain using synchrotron radiation x-rays: technical feasibility. *Nucl Instrum & Methods A* **319**, 305–310 (1992).
43. Stevenson, A. W. *et al.* First experiments on the Australian Synchrotron Imaging and Medical beamline, including investigations of the effective source size in respect of X-ray imaging. *J Synchrotron Radiat* **17**, 75–80 (2010).
44. Castelli, E. *et al.* Mammography with Synchrotron Radiation: First Clinical Experience with Phase-Detection Technique. *Radiology* (2011).
45. Carroll, F. E. Tunable monochromatic X rays: a new paradigm in medicine. *AJR Am J Roentgenol* **179**, 583–590 (2002).
46. Carroll, F. E., Mendenhall, M. H., Traeger, R. H., Brau, C. & Waters, J. W. Pulsed tunable monochromatic X-ray beams from a compact source: new opportunities. *AJR Am J Roentgenol* **181**, 1197–1202 (2003).
47. Hausser, M., Spruston, N. & Stuart, G. J. Diversity and dynamics of dendritic signaling. *Science* **290**, 739–744 (2000).
48. Scott, E. K. & Luo, L. Q. How do dendrites take their shape? *Nat Neurosci* **4**, 359–365 (2001).
49. Konnerth, A., Llano, I. & Armstrong, C. M. Synaptic currents in cerebellar Purkinje cells. *Proc Natl Acad Sci U S A* **87**, 2662–2665 (1990).
50. Hong, S. E. *et al.* Autosomal recessive lissencephaly with cerebellar hypoplasia is associated with human RELN mutations. *Nat Genet* **26**, 93–96 (2000).
51. Fatemi, S. H. Reelin mutations in mouse and man: from reeler mouse to schizophrenia, mood disorders, autism and lissencephaly. *Mol Psychiatry* **6**, 129–133 (2001).



52. Kato, M. & Dobyns, W. B. Lissencephaly and the molecular basis of neuronal migration. *Hum Mol Genet* **12 Spec No 1**, R89–96 (2003).
53. Fatemi, S. H. Reelin glycoprotein: structure, biology and roles in health and disease. *Mol Psychiatry* **10**, 251–257 (2005).

## Acknowledgments

This work was supported by the Creative Research Initiatives (Functional X-ray Imaging) of MEST/NRF, by the Swiss Fonds National de la Recherche Scientifique by the EPFL Centre d'Imagerie Biomédicale (CIBM) and by the EPFL.

## Author contributions

Guarantors of integrity of entire study, J.K., J.H.J., K.T.K., S.K., D.H., I.J.R. Y.H. and G.M. designed research; J.K., N.S.K., S.C., D.L., S.J.Y. and J.W.K. performed research; S.K., D.H.

and I.J.R. contributed new reagents/ analytic tools; J.K., N.S.K., J.H.J., D.L. and S.J.Y. analyzed data; and J.K., J.H.J., K.T.K., S.K., D.H., I.J.R., Y.H. and G.M. wrote the paper.

## Additional information

**Supplementary information** accompanies this paper at <http://www.nature.com/scientificreports>

**Competing financial interests:** The authors declare no competing financial interests.

**License:** This work is licensed under a Creative Commons Attribution-NonCommercial-ShareAlike 3.0 Unported License. To view a copy of this license, visit <http://creativecommons.org/licenses/by-nc-sa/3.0/>

**How to cite this article:** Kim, J. *et al.* Altered branching patterns of Purkinje cells in mouse model for cortical development disorder. *Sci. Rep.* **1**, 122; DOI:10.1038/srep00122 (2011).